PAPER • OPEN ACCESS

Shape resonances in angle-resolved photoionization of aligned CF$_3$I molecules

To cite this article: Felix Brausse *et al* 2023 *J. Phys. B: At. Mol. Opt. Phys.* **56** 075101

View the article online for updates and enhancements.

Shape resonances in angle-resolved photoionization of aligned CF₃I molecules

Felix Brausse[1], Marc J J Vrakking and Arnaud Rouzée*

Max-Born-Institut, Max Born Strasse 2A, 12489 Berlin, Germany

E-mail: rouzee@mbi-berlin.de

CrossMark

Abstract

The photoionization of CF₃I molecules in the photon energy range between 10 eV and 40 eV is investigated using angle-resolved photoelectron spectroscopy in the molecular frame. Using a femtosecond laser pulse, the molecules are impulsively aligned prior to their ionization by a series of extreme ultra-violet photon energies obtained by high-harmonic generation. The manifestation of molecular alignment in the photoelectron angular distributions (PADs) is well reproduced by non-relativistic quantum-mechanical photoionization calculations carried out with the ePolyScat software package, taking into account all open ionization channels. Our analysis points to two prominent shape resonances that dominate the photoelectron scattering dynamics and that therefore largely explain the observed changes in the PADs as a function of molecular alignment.

Supplementary material for this article is available online

(Some figures may appear in colour only in the online journal)

1. Introduction

The development of extreme ultraviolet (XUV) and x-ray sources has tremendously impacted our understanding of the electronic structure of matter over the course of the last century [1]. In particular, photoelectron spectroscopy using high frequency radiation has become an extremely powerful technique to measure the binding energies of electrons in atoms, molecules, and solids [2] by monitoring the kinetic energies of ejected electrons following single-photon ionization. In addition, the photoelectron angular distribution (PAD) is sensitive to both the structure of electronic continua and the shapes and symmetries of molecular orbitals [3]. Consequently, angle-resolved photoelectron spectroscopy performed in a photon energy range from the ionization threshold to the soft x-ray spectral range is particularly well suited to investigate the valence and inner-valence electronic structure of isolated molecules, providing a way to determine the binding energy and the shape and the symmetry of the molecular orbitals responsible for chemical bonding [4].

In general, the PADs contain the maximum amount of information when the photoelectrons are observed in a frame of reference in which both the molecule and the polarization vector of the light are fixed in space, which is often referred to as the molecular frame (MF) [5–7]. However, gas-phase

---

molecules rotate freely in space, and therefore most of the information content of the MF photoemission is washed out. To access the molecular-frame photoelectron angular distribution (MF-PAD) experimentally, one very successful approach consists of detecting photoelectrons and ions in coincidence and correlating the emission direction of a photoelectron with the velocity direction of an ionic molecular fragment [8–14]. In doing so, the PAD can be recovered with respect to the recoil axis in the dissociation, which is referred to as the recoil-frame-PAD. While very powerful, this technique can only be applied to molecules that do dissociate after ionization with a dissociation dynamics that needs to be fast compared to the molecular vibration and rotation. As an alternative, laser-induced molecular alignment techniques [15, 16] can be used to angularly confine the distribution of molecular orientations along specific axes. Fundamentally, the alignment is caused by the induced dipole moment that the oscillating electric field of the laser creates, mediated by the polarizability of the molecule. The torque that results from the interaction of the induced dipole moment with the laser field forces the molecules to align themselves along the laser polarization axis. Laser-induced alignment has been demonstrated using both long and ultrashort laser pulses. In the former case, the degree of alignment adiabatically follows the intensity envelope of the pulse and vanishes when the laser pulse ends [17, 18]. Consequently, the alignment can only be exploited while the alignment laser is present, which may interfere with the photoionization process one wants to characterize [19]. In the case of an ultrashort pulse, with a pulse duration much shorter than the rotational period of the molecule, a rotational wavepacket is impulsively prepared by the laser pulse, i.e. a coherent superposition of rotationally excited states that rephases periodically at well-defined time intervals after the laser pulse has ended, leading to a transient alignment of the molecules along the laser polarization axis [20, 21]. One- and three-dimensional field-free alignment of linear and (near-)symmetric top molecules has been extensively investigated [22–24], including numerous studies aiming to optimize the degree of alignment using pulse sequences and temporally-shaped laser pulses [25–32]. The technique is currently being used in a number of applications such as high-harmonic generation spectroscopy [33, 34], strong-field ionization [35–37], x-ray diffraction [38] and electron diffraction [39, 40] experiments.

In recent studies, PADs in impulsively aligned molecular ensembles have been measured for the valence-shell photoionization of linear molecules [41–44]. In these studies, an entire XUV high-harmonic comb obtained from a high-order harmonic source was used, ionizing the molecules at a series of photon energies simultaneously. Based on the changes in the PADs with molecular alignment and supported by elaborate photoionization calculations, the shapes and symmetries of the ionized orbitals were assigned. A similar experiment performed in N_2 molecules has demonstrated the possibility to completely retrieve the ionization matrix elements and to reconstruct the MF PADs of the first three ionization channels of the molecule by monitoring the PAD as a function of the laser-induced field-free alignment dynamics [45].

In the present study, the PADs resulting from XUV ionization of impulsively aligned CF_3I are investigated. CF_3I is a symmetric-top molecule, which displays a richer and more dense valence-level structure compared to linear molecules. The valence-shell photoionization dynamics of CF_3I has been the subject of several studies. Sutcliffe and Walsh [46] have investigated a series of Rydberg states converging to the ionization continuum of the ionic ground state by vacuum ultraviolet absorption spectroscopy, from which they obtained the first ionization potential of 10.41 eV. Later, Cvitas *et al* [47] provided a first assignment of the valence energy levels of CF_3I by monitoring the photoelectrons emitted by XUV ionization with He I (21.2 eV) and He II (40.8 eV) radiation. These findings were confirmed and extended by Yates *et al* [48], who recorded photoelectron spectra with synchrotron radiation, varying the photon energy between 21 eV and 100 eV. In addition, dissociative ionization of CF_3I molecules in the region of the first electronic excited state ($\tilde{A}$ band) has been extensively investigated [49, 50], including first angle-resolved photoelectron studies [12, 13, 51] based on electron-ion coincidence detection. With respect to previous studies, we recorded PADs for different ionization channels simultaneously at different photon energies. While the PADs contain a large number of ionization channels that can overlap in the presence of several harmonics in the XUV pulse, we show that in the photon energy investigated in our study, the PADs are dominated by three ionization channels, namely the $1a_2$, $3e$, and $2e$ channels, corresponding to removal of an electron from fluorine $2p$ lone-pair orbitals. The observed photon-energy dependence of the PADs for different molecular-alignment distributions is compared to and agrees reasonably well with the results of non-relativistic (NR) quantum mechanical calculations using the ePolyScat software package, taking into account a total of nine ionization channels. Our investigation reveals the presence of two shape resonances occurring at kinetic energies of $\sim$12 eV and $\sim$23 eV, which are responsible for large, characteristic modifications of the PADs observed in the experiment. The observed behavior is consistent with previous photoionization studies performed in closely related molecules such as CF_3Cl and CF_3Br [52].

2. Experiment

The XUV photoionization of CF_3I molecules was investigated using a home-built Ti:Sa laser system delivering near-infrared (NIR) pulses centered at 785 nm, with 35 fs pulse duration and a maximum pulse energy of 30 mJ at a repetition rate of 50 Hz. In this setup, up to 3 mJ of pulse energy was used to impulsively align the molecules, whereas up to 5 mJ was used to generate an XUV attosecond pulse train through high-order harmonic generation (HHG) [53, 54] in a gas cell filled with argon at a constant pressure of 80 mbar. The high-order harmonic spectrum thus generated was composed of harmonics 11 ($\approx$ 17 eV) through 31 ($\approx$ 48 eV). The intense fundamental beam was separated from the XUV beam using a 200 nm thick Al filter. The XUV beam was focused onto a molecular beam of CF_3I at the center of a velocity map imaging

(VMI) spectrometer [55], making use of a nickel-coated, grazing-incidence toroidal mirror. The molecular beam was obtained by expanding pure CF_3I, maintained at a pressure of 1 bar, through an Even–Lavie valve. Charged particles that were created upon ionization by the XUV pulse were accelerated toward a field-free flight tube that was terminated by a double-stack microchannel plate and phosphor screen assembly (MCP/Ph). The luminescence from the phosphor screen was recorded with a charge-coupled device camera. Switching the polarity of the voltages applied to the electrostatic lens of the VMI spectrometer allowed to either measure negatively or positively charged particles. Additionally, a short voltage gate was applied to the MCPs to select a specific range of mass-to-charge ratios of positively charged particles hitting the detector.

The NIR alignment pulse was stretched in a 10 cm long SF11 glass block before it was recombined with the XUV pulse using a drilled mirror. The 2 ps pulse duration of the stretched NIR pulse was characterized by monitoring the appearance of sidebands [56, 57] in the XUV ionization of helium in the presence of the NIR field. The pulse duration of the NIR laser pulse was much shorter than the rotational period of $\tau = 328$ ps of the molecule, and was responsible for the formation of a coherent rotational wavepacket. The NIR alignment pulse and the XUV pulse were co-polarized along a direction parallel to the detector plane. The delay between the pulses was controlled by a motorized delay stage. At the focus, the NIR alignment beam was characterized to be 150 μm (FWHM). Two-dimensional projections of the electron momentum distributions following XUV ionization were recorded in randomly oriented molecules and at time delays corresponding to maximum alignment and anti-alignment of the C–I bond axis along the NIR alignment laser polarization axis. The three-dimensional electron momentum distributions were then recovered using an Abel inversion procedure based on the maximum-entropy algorithm [58], from which the angle-resolved photoelectron kinetic energy spectra were extracted.

3. Computational model

All molecular photoionization calculations were carried out with the ePolyScat suite of programs developed by Lucchese *et al* [59, 60], in which the electronic structure of the molecule was treated at the Hartree–Fock (HF) level of theory. In order to approach the exact HF limit, the input HF wave functions were computed using the GAMESS (US) code (see figure 1 for the first nine valence orbitals) using the largest basis set that can be processed by ePolyScat. For all atoms, the respective all-electron basis sets of augmented quadruple-ζ quality from the Sapporo family [61, 62] of correlation-consistent Gaussian basis sets were used. The CF_3I molecule was assumed to be in its experimental equilibrium geometry taken from microwave-spectroscopy experiments [63]. Strictly, iodine is a heavy atom and therefore relativistic effects become non-negligible. Common strategies to account for heavy-atom effects are scalar-relativistic correction terms or model-core

potentials, in which the explicit treatment of the (relativistic) core electrons is avoided by replacing them with an effective potential. However, ePolyScat can neither handle model-core potentials nor does it incorporate relativistic corrections in the scattering equations. Therefore, all calculations were performed at the NR all-electron level, accepting that common relativistic effects, e. g. the uncontraction of the $4d$ shell, are not accurately reflected in the input wave function. We justify this approximation by noting that the solution of the (NR) photoelectron scattering equations largely depends on the spatial shape of the total molecular potential for energies close to the electron-impact energy. For the kinetic energies considered in this work, the effect that, the nuclear structure (i.e. bond lengths and angles) has on the shape of this potential is expected to outweigh the relatively small relativistic corrections. Nevertheless, we note that the spin–orbit coupling is known to lead to a splitting of the first cationic state of the molecule into two states [47]. However, contribution from these two ionization channels to the photoelectron spectrum is expected to be small in the photon energy range used in our study. In addition, with respect to the large bandwidth of the XUV pulse used in our study, it will be very difficult to resolve such splitting in the condition of our experiment.

In the ePolyScat calculations, the basis set and the orbital coefficients from the HF calculation were read in and the HF orbital wave functions ϕ_i^{HF} were re-expanded onto a spherical grid by a single-center expansion into a basis set of spherical harmonics with a maximum angular momentum l_{max}. To reach convergence, photoionization calculations were performed for CF_3I with a maximum angular momentum of $l_{max} = 70$ and the center located 1.80 Å away from the carbon atom along the carbon–iodine bond (hence at a distance of 0.314 Å from the iodine atom). For the chosen maximum angular momentum $l_{max} = 70$, the average error introduced by truncating the expansion was $\approx 0.5\%$ for all orbitals and $<0.1\%$ for the valence levels, in particular. Following the re-expansion of the HF wave functions ϕ_i^{HF}, all allowed continuum transitions from the nine molecular valence orbitals (see figure 1) of the molecule by harmonics 11 through 31 were evaluated within the full exact-static–exchange-plus-model-correlation–polarization model (ESECP). Within the dipole approximation, the photoionization matrix elements for these transitions were calculated using the dipole overlap between the HF molecular orbitals ϕ_i^{HF} and the continuum wave functions $\psi_i(\epsilon)$ for an electron with kinetic energy ϵ scattering off CF_3I^+ in which one electron was removed from orbital i. These overlap matrix elements can be written as $\langle \phi_i^{HF} | d_{V,L} | \psi_i(\epsilon) \rangle$ where $d_{V,L}$ is the dipole operator in either position space (length gauge, L) or momentum space (velocity gauge, V). With the model-correlation potential used here, calculations performed using the two gauges deviated by less than 5%. In what follows, if no gauge is mentioned, the average between the results obtained using the two gauges was used.

The photon energies and amplitudes of harmonics 17 through 31 were taken from a measurement of the photoelectron spectrum recorded in helium that is shown in figure 2, from which the harmonics spectrum was reconstructed using the known values for the ionization cross section
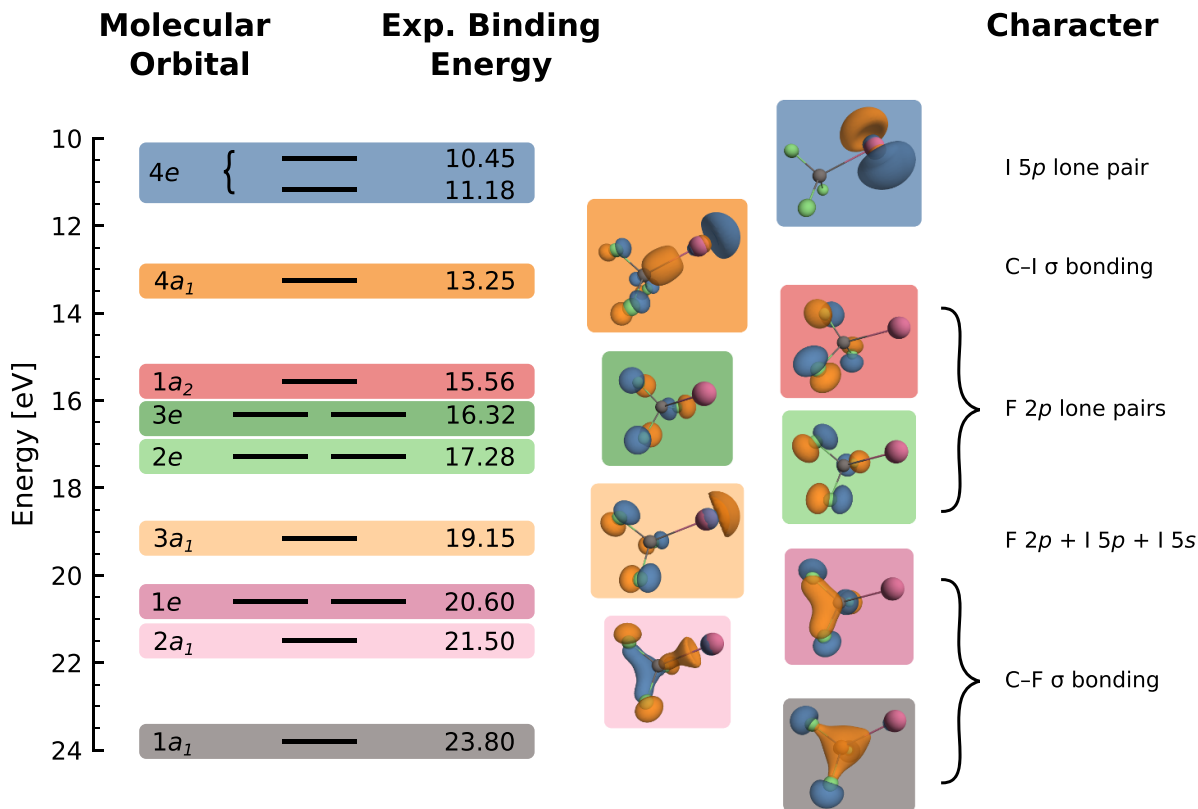
J. Phys. B: At. Mol. Opt. Phys. **56** (2023) 075101

F Brausse *et al*

Figure 1. Electronic structure of CF_3I. The binding energies and molecular-orbital assignments are taken from Yates *et al* [48]. Calculated Hartree–Fock orbitals are shown as isocontour surfaces at a wave function value of $\pm 0.1 a_0^{3/2}$. Reproduced with permission from [64].
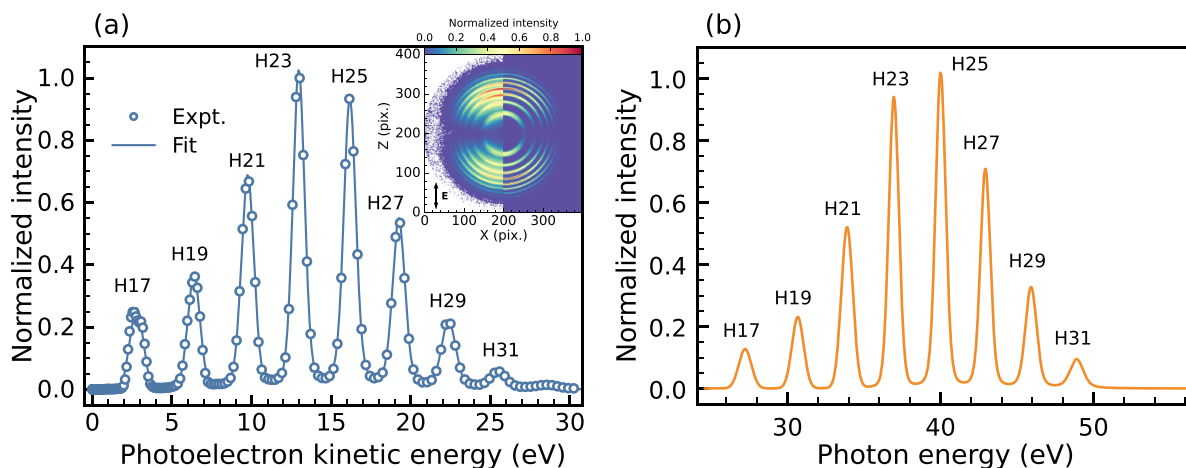

Figure 2. (a) Angle-integrated photoelectron spectrum recorded for the ionization of helium by the HHG pulse (open circles) and corresponding fit (line). The inset shows a slice through the 3D electron momentum distribution recorded in helium. (b) Reconstructed HHG spectrum obtained from the fit using the photoionization cross sections of helium reported by Samson and Stolte [65]. Reproduced with permission from [64].

of helium [65]. For lower harmonics, they were estimated as $N\hbar\omega_{eff}$, with N the harmonic order. For the construction of the model polarization potential, the polarizability tensor was calculated *ab-initio* using the GAMESS (US) code. At the CCSD(T)/MCP-ATZP level of theory, static-field calculations (see table 1) carried out for a set of increasing strengths of an electric field applied along the Cartesian axes yielded the components of the static polarizability as $a_{zz} = 9.04$ Å^3

and $a_{xx} = a_{yy} = 6.67$ Å^3 (with the z axis being parallel to the principal molecular axis). For the model correlation potential, the Padial–Norcross functional [66] was employed, which was specifically developed for describing the electron correlation in electron–molecule collisions.

To benchmark the fidelity of our photoionization calculations, the branching ratios for ionization into a final state f in a photon energy range from the ionization threshold to 50 eV

Table 1. Calculated components of the dipole moment, μ_i, and the polarizability tensor, α_{ii}.

	μ_z (D)	μ_x (D)	α_{zz} (Å³)	$\alpha_{xx} = \alpha_{yy}$ (Å³)	$\langle\alpha\rangle$ (Å³)
This work	1.0540	0.000[a]	9.04	6.67	7.46
Reference	1.048(3)[b]				8.90[c]

[a] As required by symmetry.
[b] From microwave spectroscopy, [63].
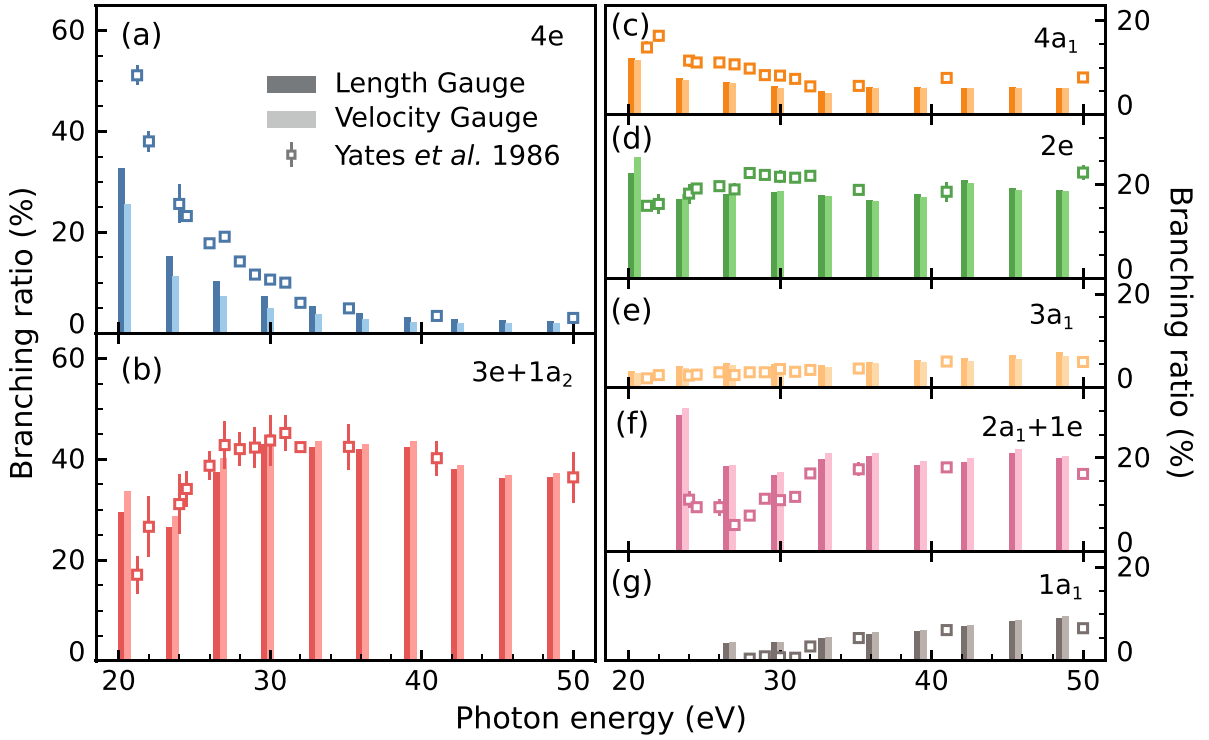[c] Value extrapolated by [67] from the series of CF₃X molecules, with X = H, F, Cl, Br, I.

Figure 3. Branching ratios for the valence-shell photoionization of CF₃I. Vertical bars show the results from the ePolyScat calculations in the length gauge (darker shading) and the velocity gauge (lighter shading), respectively. For comparison, experimental values from Yates *et al* [48] (open squares) are shown together with their reported experimental uncertainty. To emphasize the relative strength of the contributions, all panels are to scale with respect to each other. Reproduced with permission from [64].

were evaluated and compared to the synchrotron studies by Yates *et al* [48] (see figure 3). The branching ratios were calculated by taking the ratio between the ionization cross-section obtained for a specific ionization channel with respect to the sum over the total ionization cross-section, including all ionization channels. Overall, a very satisfying agreement between the calculations and the experiment is observed. We note nevertheless that, just above the ionization threshold, the calculated branching ratios are slightly overestimated. We explain this behavior by a strong one-electron resonance for photoelectrons with 1 eV of kinetic energy that appears in different channels in the calculation (mainly seen in panels (b) and (f) of figure 3) and that is not observed at this specific energy in the experiment of Yates *et al* [48]. Potentially, this is a consequence of the total neglect of relativistic effects in our calculations. However, this effect occurs at kinetic energies well below the ones discussed in the experimental results presented here.

The angle-resolved photoelectron spectrum $F(\epsilon_k, \Omega)$ resulting from the ionization of CF₃I by the harmonics comb as a function of the photoelectron kinetic energy ϵ_k and photoemission angle Ω was computed using the following expression:

$$F(\epsilon_k, \Omega) = \sum_N \sum_f \left(d\sigma_f(\epsilon_f^{(N)})/d\Omega \right) \frac{I^{(N)}}{k}$$

$$\times \exp\left[\frac{-(\epsilon_k - \epsilon_f^{(N)})^2}{2k^2} \right] \tag{1}$$

where $\epsilon_f^{(N)}$ is the kinetic energy of the photoelectron after ionization of the molecule by the Nth harmonic into the final state f, and σ and $I^{(N)}$ are the width and the amplitude of the Nth harmonic, respectively. In our calculation, we assumed the width to be constant and treated it as a free fitting parameter. $\sigma_f(\epsilon_f^{(N)})$ is the ionization cross section into the final state f. The

differential ionization cross section in the laboratory frame, $d\sigma_f(\epsilon_f^{(N)})/d\Omega$ was then calculated by a convolution of the doubly differential ionization cross section $d\sigma_f(\epsilon_f^{(N)}, \mathbf{R})/d\Omega$, with the molecular-axis probability distribution, P_{MA}, of the molecular ensemble:

$$\frac{d\sigma_f(\epsilon_f^{(N)})}{d\Omega} = \int_0^\pi \int_0^{2\pi} P_{MA}(\beta) \frac{d\sigma_f(\epsilon_f^{(N)}, \mathbf{R})}{d\Omega} d\alpha d\beta , \quad (2)$$

where $\mathbf{R} = (\alpha, \beta, \gamma)$ is the set of Euler angles defining the transformation between the fixed-in-space MF and the laboratory frame.

4. Laser-induced field-free alignment dynamics

The laser-induced field-free alignment dynamics of CF_3I molecules was characterized by monitoring the angular distribution of I^+ ion momentum distributions resulting from dissociative ionization of the molecules by the XUV harmonic comb using the procedure introduced in [44]. Figure 4 displays a typical 2D I^+ momentum distribution recorded without the alignment laser pulse as well as the corresponding angle-integrated kinetic energy spectrum. Several features are apparent: an intense feature in the center of the distribution (labeled A in figure 4(a)) with a corresponding kinetic energy that peaks at 0.17 eV, a broad rim that falls off slowly (labeled B), with a corresponding mean kinetic energy of 0.43 eV and a concentric ring (labeled C), with a corresponding kinetic energy of 2.2 eV. Assuming momentum conservation, the I^+ fragment kinetic energies of 0.17 eV, 0.43 eV and 2.2 eV correspond to total kinetic energy releases (KER) of 0.43 eV, 1.33 eV and 6.3 eV, respectively.

The I^+ fragments with a kinetic energy of 0.17 eV have been previously observed, albeit at a lower photon energy of 15 eV, and assigned to dissociative ionization of CF_3I involving the $\tilde{A}$ cationic state [49] leading to a neutral CF_3 fragment and a singly charged iodine ion. Dissociative ionization from higher excited states is responsible for the formation of I^+ fragments with higher kinetic energies. In particular, dissociative ionization involving the $\tilde{E}$ cationic state is known to produce fragments with a total KER of 0.69 eV. This fragmentation channel is likely the dominant process responsible for the appearance of the shoulder observed in the I^+ kinetic energy spectrum near 0.43 eV. We note nevertheless that at the high photon energy used in our experiment which extends up to 50 eV, a large number of dissociative ionization channels can be responsible for the formation of I^+ fragments and can have a non-negligible contribution to the two channels labeled A and B in the measured I^+ kinetic energy distribution. The weaker contribution, labeled C, with a kinetic energy of 2.2 eV can be assigned to Coulomb explosion following double ionization of CF_3I. The total KER of these fragments is close to the Coulomb repulsion energy $q_1 q_2/R_e = 6.72$ eV of two point charges with charge $q_1 = q_2 = 1$, separated by the equilibrium C–I bond length of CF_3I, $R_e = 2.144$ Å. The appearance threshold for the $CF_3^+ + I^+$ channel has been estimated

to be ≈ 31 eV [68], and can therefore be accessed with all harmonics above and including harmonic 21.

At a pump–probe delay of 162.5 ps, a strong angular confinement of the I^+ fragment momentum distribution is observed in all ionization channels, which is a direct manifestation of the alignment of the molecules along the NIR alignment laser polarization axis. In the axial recoil approximation, i.e. assuming that the dissociation of the molecular ion is fast with respect to the vibrational and rotational motion [69], the molecular axis distribution of the molecule at the time of ionization is directly imprinted onto the angular distribution of the charged fragments. This is clearly observed in figure 4(b), which displays the time-dependent fragment-ion angular distribution integrated over a kinetic energy range from 0.40 eV to 0.65 eV (region B in figure 4) in the time interval from 158 ps and 170 ps, i.e. around the first revival of the rotational wavepacket that is prepared by the alignment laser pulse. Region B was chosen over the Coulonb-explosion channel (region C) due to the increased signal-to-noise ratio observed in this channel. The fragment angular distribution in this kinetic energy range quickly evolves from a distribution that peaks at $\theta = (0, \pi)$, i.e. along the NIR laser pulse polarization axis, at a time delay of 162.5 ps, to a distribution that peaks at $\theta = \pi/2$, i.e. perpendicular to the NIR laser pulse polarization axis, at a time delay of 165.5 ps.

To characterize the molecular-axis probability distribution $P_{MA}(t, \theta)$ observed experimentally, we assume that the ion momentum distribution $I(p, t, \theta)$, which is a function of the ionic fragment's drift momentum p and the angle θ between the polarization axis of the incident radiation and the direction of the drift momentum, can be written as:

$$I(p, t, \theta) = P_{MA}(t, \theta) d\sigma_{ion}/d\theta. \quad (3)$$

$d\sigma_{ion}/d\theta$ is the differential ion yield for a given ionization channel given by:

$$d\sigma_{ion}/d\theta = \sigma_{ion}(p)[1 + \beta_{ion}(p)P_2(\cos\theta)] \quad (4)$$

with β_{ion}, the asymmetry parameter describing the parallel/perpendicular character of the transition leading to a fragment with a final momentum p and $P_2(\cos\theta) = (3\cos^2\theta - 1)/2$. A least-squares fitting minimization was used to fit the result of a simulation of equation (3) to the experimental time-dependent ion momentum distribution. In the simulation, the molecular-axis probability distribution $P_{MA}(t, \theta)$ was computed numerically by solving the time-dependent Schrödinger equation in the rigid rotor approximation using the rotational temperature T and the NIR laser intensity I_0 as fitting parameters [70]. A very good agreement was achieved for $T = (19.2 \pm 0.5)$ K, $I_0 = (2.3 \pm 0.1) \times 10^{12}$ W cm^{-2} and $\beta_{ion} = 0.64 \pm 0.02$, see figure 4(b) through (d). Based from our fit, we estimated a maximum degree of alignment and anti-alignment reached experimentally of $\langle\cos^2\theta\rangle = 0.65$ and $\langle\cos^2\theta\rangle = 0.3$, respectively.
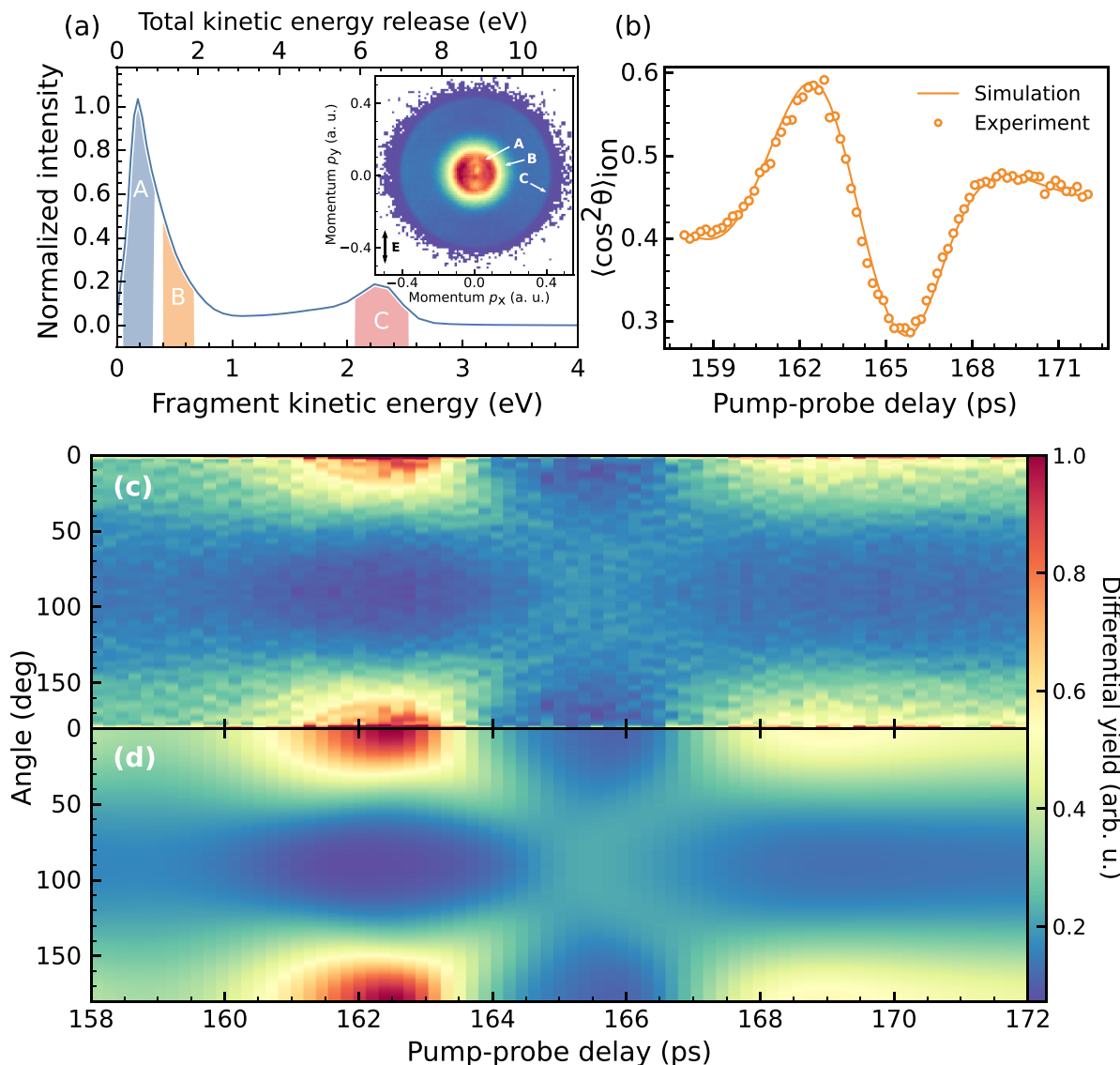
Figure 4. (a) Kinetic-energy distribution of I^+ fragments resulting from ionization of CF_3I molecules by the harmonic comb. The inset displays the corresponding 2D I^+ momentum distribution recorded with the VMI spectrometer. A: fragments resulting from the dissociation of low-lying ionic states of CF_3I^+; B: fragments associated with the dissociation of highly excited states of CF_3I^+; C: Coulomb explosion fragments from the dissociation of CF_3I^{2+} into $CF_3^+ + I^+$. (b) Evolution of the expectation value $\cos^2 \theta_{ion}$ of the reconstructed, three-dimensional ion momentum distributions as a function of the pump–probe delay, integrated in the kinetic energy region marked as B. (c), (d) Measured (c) and calculated (d) evolution of the fragment-ion angular distribution for the data of panel (b) as a function of the pump–probe time delay near the first revival of the rotational wavepacket. Reproduced with permission from [64].

5. Angle-resolved photoelectron spectrum of CF₃I

Electron momentum distributions recorded at pump–probe delays corresponding to maximum alignment and maximum anti-alignment, i.e. at 162.5 ps and 165.5 ps, respectively, are shown in figures 5(a) and (b). The left halves display the recorded 2D electron momentum distributions whereas slices through the 3D electron momentum distributions retrieved after an Abel inversion are shown in the right halves. For the two alignment distributions, the momentum distributions are composed of concentric rings that can be assigned to ionization of various molecular orbitals by the harmonics comb. The angle-integrated photoelectron spectra shown in figure 5(d)

indicate that ionization mainly involves three ionization channels, $2e$, $3e$ and $1a_2$, which correspond to the ionization of fluorine $2p$ lone-pair orbitals. At a photon energy of 30 eV, we expect these three channels to account for more than 60% of the overall ionization yield (see figure 3 and [48]). As shown in figure 5(d), many of the peaks in the photoelectron spectra coincide with these state assignments. In the region from 5 to 20 eV, ionization is dominated by the $2e$ orbital, whereas from 20 eV upwards, the $3e$ orbital has the highest contribution. We note that below 5 eV, the electron momentum distributions are dominated by contributions from above-threshold ionization induced by the alignment laser pulse. Therefore this region will not be discussed any further.
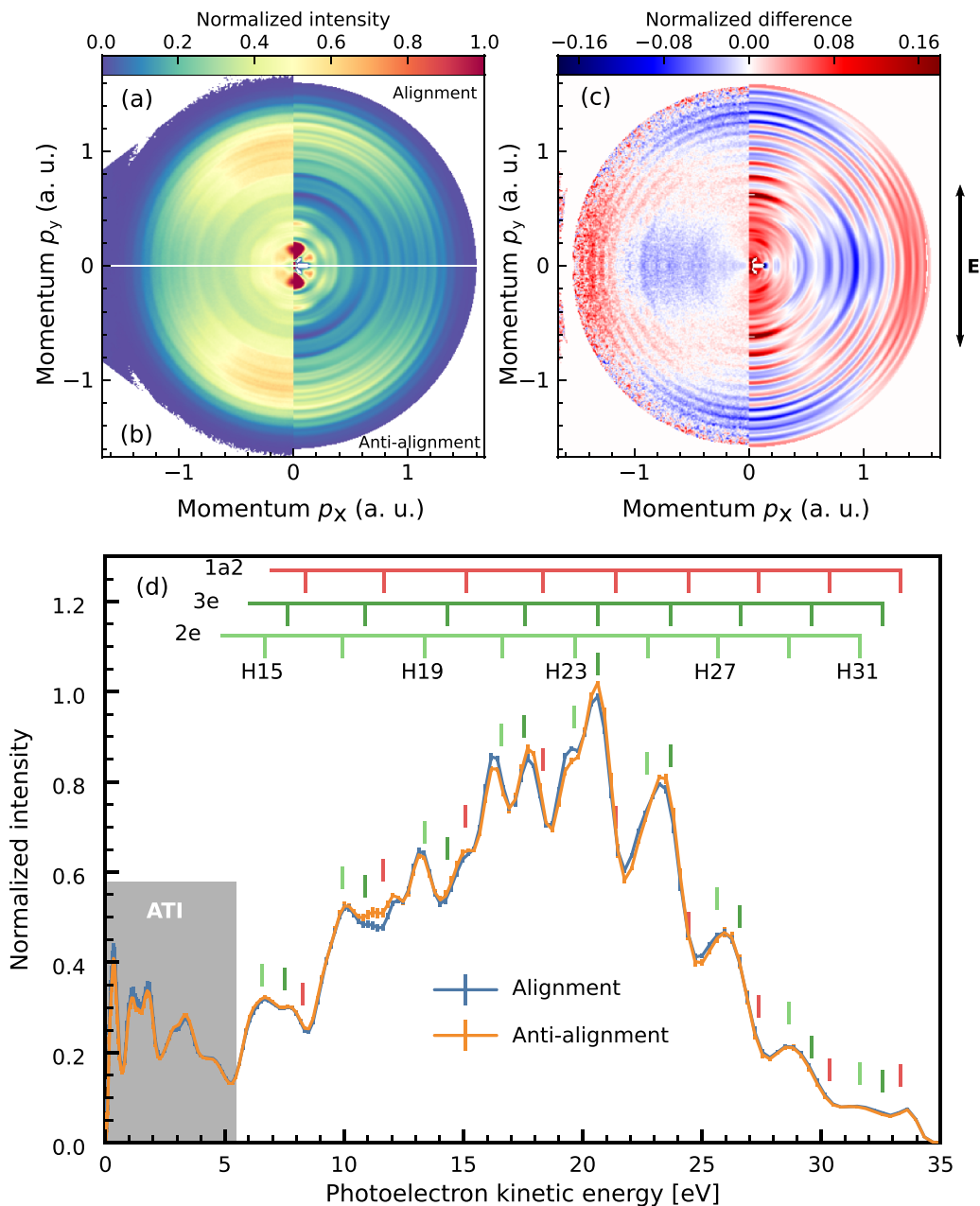
Figure 5. 2D detector images (left halves) and slices through the 3D velocity distributions (right halves) for the photoionization of pure CF$_3$I by the XUV harmonic comb. (a), (b) Comparison between data recorded at the alignment peak (a, $\tau = 162.5$ ps) and the maximum anti-alignment (b, $\tau = 165.5$ ps). (c) Normalized difference between (a) and (b) according to equation (5). For visualization purposes, the quadrants were mirrored vertically in c. (d) Corresponding normalized angle-integrated electron kinetic energy spectra recorded at the maximum of alignment (blue line) and anti-alignment (orange line). The scales at the top indicate the theoretical peak positions of photoelectron lines resulting from ionization of the three indicated orbitals. Small vertical dashes are intended to serve as a guide to the eye. We note that the signal below 5 eV (grey box) is dominated by above-threshold ionization (ATI) from the 800 nm alignment laser pulse. Reproduced with permission from [64].

The electron momentum distributions recorded for molecules with distinct molecular-axis distributions appear—to the eye—very similar due to the relatively low degree of alignment and anti-alignment achieved experimentally. The PAD of the ejected electrons at all kinetic energies are only slightly affected by the alignment distribution of the molecule (see also figure 3 of the supporting material). However, pronounced variations are observed in the normalized difference of the momentum distributions displayed in figure 5(c) and calculated according to:

$$I = \frac{I_{\mathrm{A}} - I_{\mathrm{AA}}}{I_{\mathrm{A}} + I_{\mathrm{AA}}} \qquad (5)$$

with I_{A} and I_{AA}, the momentum distributions recorded for molecules aligned and anti-aligned, respectively. At certain
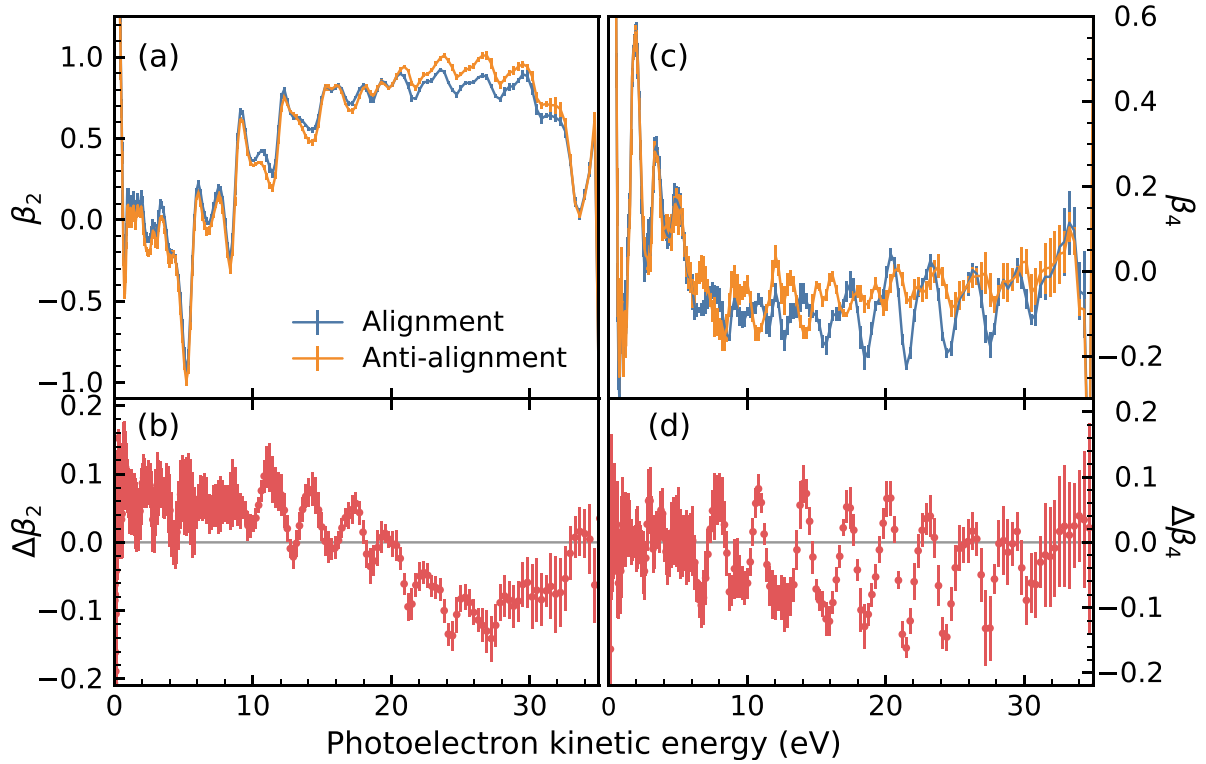
Figure 6. Kinetic energy dependence of the β_l parameters. (a) β_2 as a function of the electron kinetic energy for molecules aligned (blue line) and anti-aligned (orange line) with respect to the XUV polarization axis. (b) Absolute difference, $\Delta\beta_2$, between the two measurements shown in (a). (c), (d) Same as (a) and (b) for the β_4 parameter. Error bars correspond to confidence intervals of 95%. Reproduced with permission from [64].

kinetic energies, a clear variation of the electron signal, with up to a 16% modulation, is observed. At a momentum below 0.8 a.u., a strong enhancement and a depletion of the electron signal is observed along and perpendicular to the laser polarization axis, respectively. An opposite behavior is observed at a momentum of 1 a.u. and above. A large increase of the electron signal at an emission angle of 45° is also noticeable in an intermediate momentum region between 0.8 a.u. and 1 a.u., which suggests the presence of higher-order angular momenta in the normalized difference map.

For a sample of isotropically distributed molecules, the electron angular distribution is generally characterized by a single angular asymmetry parameter β and the PAD is described using:

$$I(\theta) = \sigma_0(1 + \beta P_2(\cos\theta)) \qquad (6)$$

with $P_2(\cos\theta)$, the second order Legendre polynomial and σ_0, the ionization cross-section. However, for a sample of aligned molecules, the PAD takes the general form [7]:

$$I(\theta) = \sum_L B_L P_L(\cos\theta) = \sigma_0(1 + \beta_2 P_2(\cos\theta)$$
$$+ \beta_4 P_4(\cos\theta) + \dots) \qquad (7)$$

with β_n, the angular asymmetry parameters and $P_n(\cos\theta)$ the Legendre polynomials. This expression characterizes the laboratory-frame PAD as a convolution of the PAD in the MF

and the molecular-axis distribution. In the limit of a perfect degree of alignment, the PADs in these two frames essentially converge. Still, even at a moderate degree of alignment, important qualitative features of the MF-PAD features and their energy dependence manifest in the laboratory frame.

The angular asymmetry parameters extracted from our measurement by fitting the photoelectron kinetic-energy distributions recorded at maximum alignment and anti-alignment using the equation (7) are shown in figure 6. In addition, their corresponding absolute differences, $\Delta\beta_l$, are also shown. Here, we restrict the discussion to β_2 and β_4, as the changes in β_6 and higher were too small to be detected in the present experiment. For molecules aligned and anti-aligned with respect to the XUV polarization axis, the photoelectron spectra are characterized by a positive β_2 contribution at all kinetic energies. In addition, we observe that the β_2 contribution increases substantially from almost 0 to 1 in the kinetic energy range between 5 eV and 30 eV. The positive β_2 contribution observed experimentally and its increase with the photon energy suggests that single photon ionization in a photon energy range covered by the harmonic comb favors parallel transitions. In addition, the β_4 distribution for aligned molecules shows pronounced oscillation around zero, while it remains quasi constant for anti-aligned molecules. Interestingly, in the photon energy range between 11 eV and 27 eV, the difference $\Delta\beta_2$ shown in figure 6 is clearly changing sign from a positive value of 0.1 near 11 eV to a negative value of -0.1 at 27 eV, on top of which a faster oscillation appears.

This is consistent with the trend that was already discussed in connection with figure 5(c).

To understand the dependence of the experimental angle-resolved photoelectron spectrum on the molecular alignment, the doubly differential photoionization cross sections computed for photoionization of CF$_3$I using ePolyScat (see section 3) were convoluted with the alignment distributions obtained from the ion measurements of figure 4 by making use of equation (2). The resulting differential cross sections were combined according to equation (1) to yield simulated, angle-resolved photoelectron spectra. A comparison between the experimentally recorded and simulated photoelectron spectrum obtained at maximum alignment is displayed in figure 7. We note that only the amplitude of harmonics 11 to 15 were fitted in our model. For higher harmonics, the amplitudes were taken from the reconstructed harmonic spectrum (see figure 2).

In the inset of figure 7(a), the relative intensities of the entire harmonic comb are shown, and it appears that the strengths of the fitted harmonics smoothly match the reconstructed spectrum. The overall structure of the angle-integrated photoelectron spectrum displayed in figure 7(a) is qualitatively well reproduced by our model. We nevertheless note the systematic overestimation of the total ionization cross section with increasing photoelectron kinetic energy in our model. In the spectra, which are normalized to maximum peak height, this leads to the observation that the calculated photoelectron spectrum is smaller than the measured one below the normalization point, and more intense above it. For the asymmetry parameter β_2 displayed in figure 7(b), however, we find an almost quantitative agreement between the experimental and the calculated β_2 in the kinetic-energy range between 5 eV and 30 eV. A comparison between the measured and calculated normalized difference between the angle-resolved photoelectron spectra taken at maximum alignment and maximum anti-alignment are shown in figure 7(c). In addition, calculated channel-resolved cross-sections and β_2 parameters for an aligned and anti-aligned molecular ensemble are presented in the figure 1 of the supporting material (SM), together with channel-resolved difference of photoelectron kinetic energy distributions (see figure 2 of SM). Considering the number of ionization channels and simplifications made in the model, we find that the measured differential angle-resolved photoelectron spectrum shown in figure 7(c) is rather well reproduced by the simulation. In particular, the characteristic, repetitive angular pattern between 15 eV and 30 eV is almost quantitatively matched.

Interestingly, our model also reproduces the kinetic energy dependence of the *absolute* difference (i.e. between the case of maximum alignment *minus* the one of maximum anti-alignment) of the asymmetry parameters $\Delta\beta_l$. Our simulation shown in figure 8(a) reproduces the change in the sign of $\Delta\beta_2$ that occurs in the kinetic energy range between 15 eV and 25 eV quite well. This trend disappears when the photoelectron—molecular-ion interaction is switched off in our model by using Coulomb waves [71] as final states instead of the scattering solutions $\psi_i(\epsilon)$ (figure 8(c)). This suggests
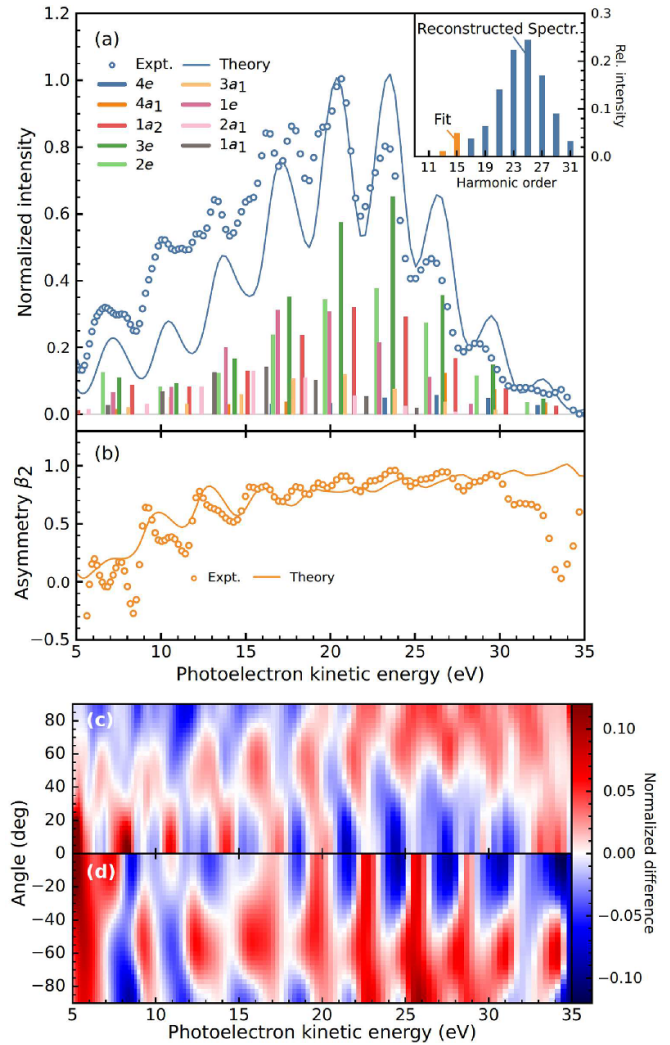

Figure 7. (a) Comparison between the experimental (open circles) and simulated (solid line) normalized angle-integrated photoelectron spectrum taking into account the experimentally obtained harmonics spectrum. The experimental photoelectron spectrum was taken at the maximum molecular alignment. The simulated spectrum was obtained from equation (2) using the alignment distribution P_{MA} characterized experimentally. A decomposition into the individual contributions is shown as a stick spectrum. The inset shows the complete harmonics spectrum, distinguishing between the harmonics that were obtained from a fit (orange) and those that were obtained from the photoelectron spectrum in helium (blue, see section 3). (b) Same as (a) for the asymmetry parameter β_2. (c), (d) Comparison between the measured (c) and calculated (d) normalized difference between angle-resolved photoelectron spectra taken at maximum alignment and maximum anti-alignment. Reproduced with permission from [64].

that the electron scattering interaction is key to understanding this effect. By contrast, in the Coulomb-wave approximation [71], the rapidly oscillating modulations observed experimentally both in $\Delta\beta_2$ and $\Delta\beta_4$ are still observed. We therefore conclude that these oscillations are not determined by the electron scattering interaction. Instead, the period of the fast oscillation observed in the β_2 parameter follows the minima and maxima in the photoelectron spectrum. These oscillations can
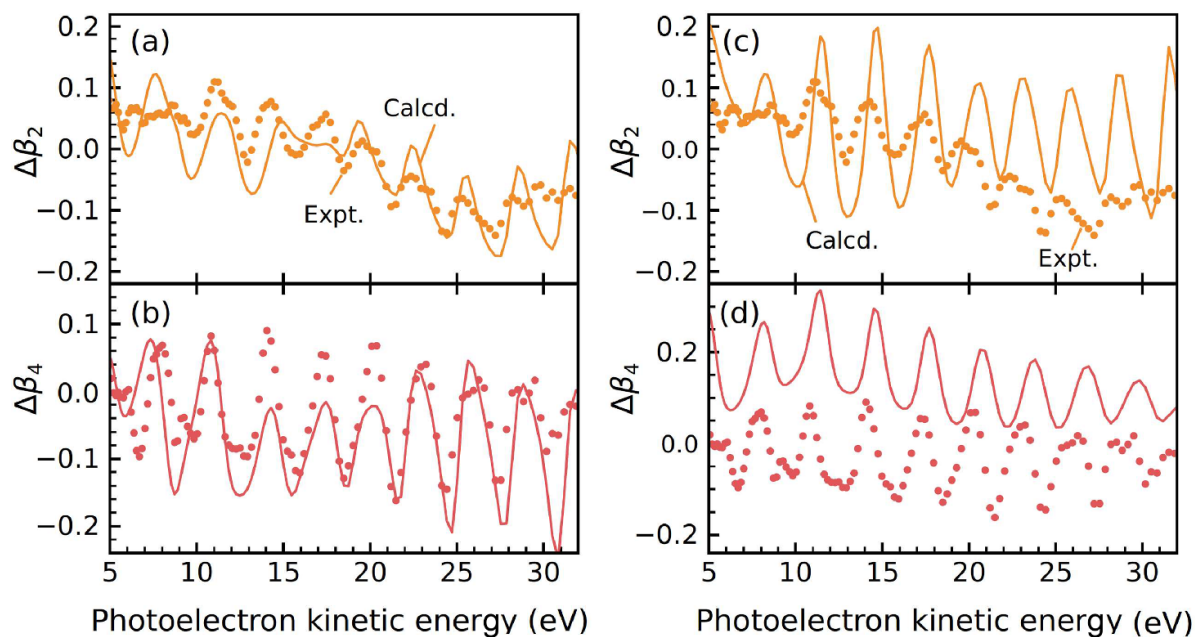
Figure 8. Comparison between the experimental and theoretical kinetic energy dependence of $\Delta\beta_l$. (a), (b) Comparison between the experiment (dots) and the full ePolyScat model (solid lines). (c), (d) Same as (a) and (b) but for the calculation with Coulomb waves instead of the full model. Reproduced with permission from [64].

be largely explained by the different shapes of the molecular orbitals (and in particular the F 2p lone pairs orbitals that have the highest contribution to the photoelectron spectrum) which lead to different dipole transition preferences that create a pattern that repeats with the spacing of the HHG pulse.

We tentatively propose that the change of the angular distribution occurring between 15 eV to 25 eV is indicative of underlying one-particle resonances, typically referred to as 'shape resonances'. Previous studies have discussed the presence of shape resonances in the photoionization of CF_3I [13] and CF_3Cl [72] lying 2–3 eV above the ionization threshold. In CF_3Cl, the origin of the shape resonance was attributed to a trapping mechanism of the photoelectron around the CF_3 group. Also, a second shape resonance in the 13–15 eV kinetic energy region was discussed by Yates *et al* [48] which was responsible for a weak shoulder in the total ionization cross section. A shape resonance can be described as the transient trapping of the departing photoelectron by a centrifugal barrier and manifests as a sudden jump in the eigenphase sum for the electron scattering off the target ion [73]. A shape resonance is generally accompanied by a large increase of the ionization cross-section as well as a drastic change of the angular distribution of the ejected photoelectron.

To characterize the exact shapes of the resonance wave functions and hence their potential impact on the PADs, we show in figure 9 the calculated eigenphase sum for the $3e$ channel over the energy region of interest. Notably, not just one, but two steep rises are observed, at energies of $E_1 = 12.0$ eV and $E_2 = 23.4$ eV, respectively.

Formally, shape resonances are defined as poles of the scattering S matrix when its energy dependence is analytically extended into the complex plane [73, 74]. Resonance energy E and width Γ of the pole are related to the real and complex parts of the pole energy as $E - i\Gamma/2$. To characterize the shape resonances that are involved, we have carried out pole searches in the complex scattering-energy plane with the algorithm developed by Stratmann and Lucchese [75]. When a resonance is found, the associated scattering wave function can be evaluated at the complex-valued energy which is then equal to the *pure* resonance wave function.

For the resonance search, a simplified, static potential with model exchange is used, which is energy independent, in contrast to the more sophisticated ESECP model introduced above (see also [76] and its supplementary material for details on the pole-searching calculations). From the resonance search we are able to identify two poles that correspond closely in energy and width to the phase jumps observed in figure 9(a) ($E_1^{\text{pole}} = 11.1 - 2.7i$ eV, $E_2^{\text{pole}} = 23.1 - 3.2i$ eV). The corresponding resonance wave functions are displayed in figures 9(c) and (d).

To demonstrate that these shape resonances significantly modulate the PADs, we compare the MF-PAD at harmonic 19 (13.5 eV, figure 9(e)) and 25 (22.9 eV, figure 9(f)), which are closest to the determined resonance positions, to the asymptotic shapes of the resonance wave functions. Clearly, there is a striking similarity between the MF-PAD and the asymptotic behavior of the resonance wave functions (panels (c) and (d) in figure 9). The shape resonance at 12 eV leads to an enhanced ionization along the C–I bond coordinate and we therefore
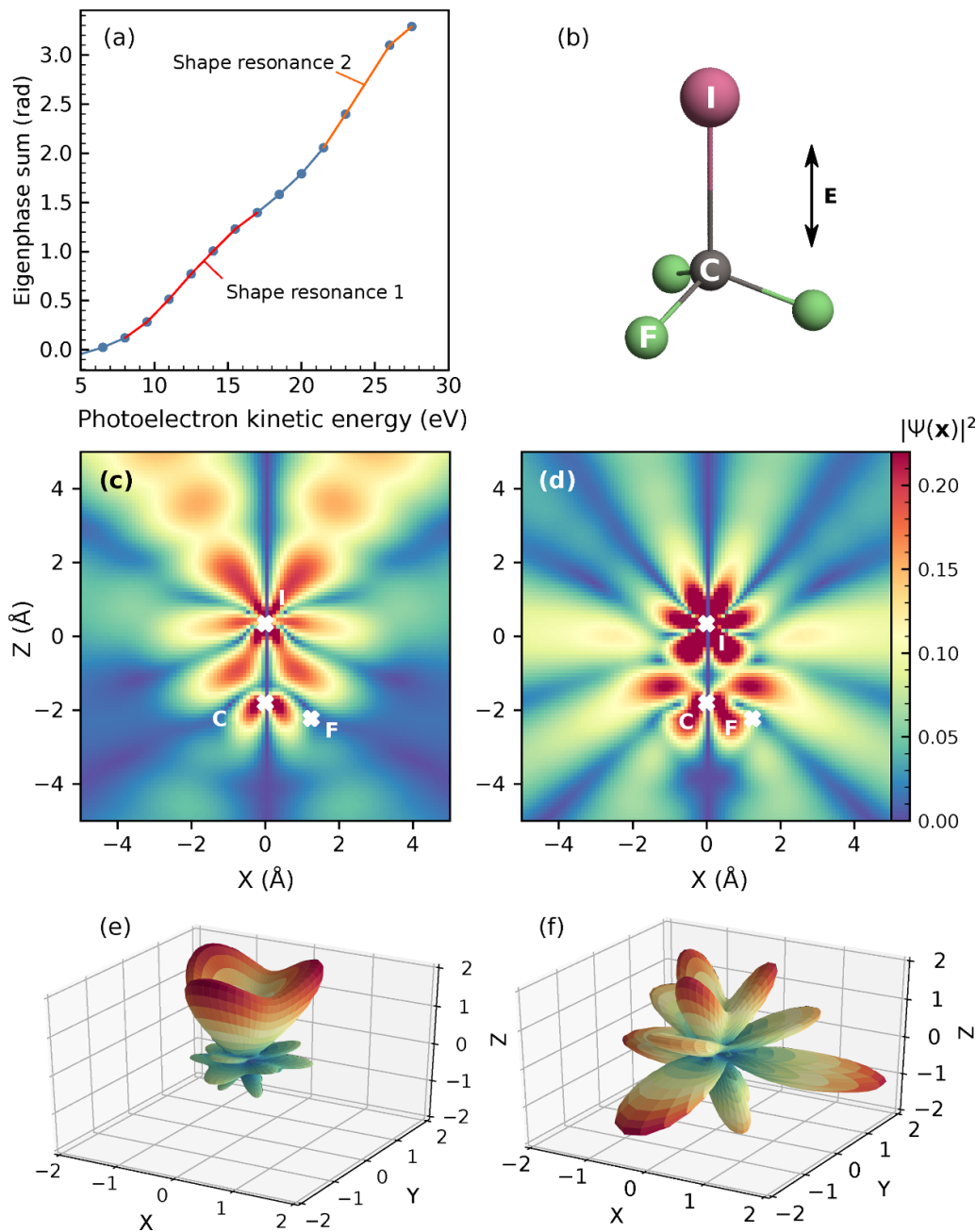
J. Phys. B: At. Mol. Opt. Phys. **56** (2023) 075101

F Brausse *et al*

Figure 9. Characterization of the shape resonances in the photoionization of the $3e$ channel of CF_3I. (a) Eigenphase sum for the electron scattering off CF_3I^+ ($3e^{-1}$)) (dots). (b) Sketch of the CF_3I molecule and its orientation in the molecular frames of panels (c) through (f). (c), (d) Resonance wave functions in the $3e \rightarrow ke$ photoionization of CF_3I. Real part of the resonance wave functions at $E = 11.1 - 2.7i$ eV (c) and $E = 23.1 - 3.2i$ eV (d), shown as cuts through the Cartesian $x - z$ plane that contains the iodine, carbon atoms and one fluorine atom (marked by crosses). (e), (f) Molecular-frame photoelectron angular distributions (in units of Mb sr^{-1}) for photoionization with harmonic 19, close to the resonance of (c) and for harmonic 25, close to the resonance of (d). Reproduced with permission from [64].

expect an increase of the β_2 parameter when the molecules are aligned along the laser polarization. In contrast, the shape resonance near 23 eV is leading to an emission perpendicular to the C–I bond axis. We expect therefore that at this kinetic energy, the β_2 parameters will be higher when the molecules are aligned perpendicularly to the laser polarization axis. From this and from the asymptotic shapes of the resonances discussed above, we conclude that the change in sign of $\Delta\beta_2$ from positive to negative with increasing photoelectron kinetic

energy (see figure 8(a)) can be explained by the presence of the two shape resonances.

6. Conclusion

In this work, we have investigated PADs in the XUV ionization of aligned CF_3I. To guide the interpretation of the photoelectron measurements, photoionization calculations

were performed for all open ionization channels. A rather good agreement was observed between the experiment and the calculation, within the known limitations of the theoretical model. The detailed analysis of the alignment-dependent changes in the PADs gives strong evidence that the observed changes can, to a large extent, be understood from the contributions of two prominent shape resonances that are not directly apparent in the photoelectron spectra of the unaligned molecules. This interpretation is supported by the observation that the measured trends in the energy dependence of the angular-distribution parameters cannot be reproduced when photoelectron scattering is turned off completely, which of course eliminates any scattering resonance. Our findings show that the introduction of molecular alignment can reveal, even when facing convoluted spectra from molecules with dense valence-level structures, details of the photoelectron scattering process that would remain elusive otherwise. Our investigation shows that it is possible to reveal the general structure of the photoelectron scattering dynamics even though many open channels and photon energies were involved in the experiment. The analysis was possible because the same or very similar shape resonance manifest in different ionization channels, especially if the ionized orbitals have a similar quality (like the fluorine lone pairs here). Therefore, similar modulations in the PADs will appear at comparable kinetic energies in different ionization channels and the contributions add up. This observation has important consequences for attosecond experiments which require XUV pulses with very broad bandwidths. Our findings suggest that, even when it is very difficult to disentangle individual ionization channels, the photoelectron scattering dynamics potentially reveal themselves in the experiment through strong shape resonances.

Data availability statement

Acknowledgments

ORCID iD

Arnaud Rouzée ⓘ https://orcid.org/0000-0002-2425-4027

References

[1] Stöhr J 1992 *Nexafs Spectroscopy* (*Springer Series in Surface Sciences*) vol 25 (Berlin: Springer)
[2] Jenkin J, Leckey R and Liesegang J 1977 *J. Electron. Spectros. Relat. Phenomena* **12** 1–35
[3] Berkowitz J 1979 *Photoabsorption, Photoionization and Photoelectron Spectroscopy* (New York: Acad-Press)
[4] Price W C 1981 *Int. Rev. Phys. Chem.* **1** 1–30
[5] Dill D 1976 *J. Chem. Phys.* **65** 1130–3
[6] Chandra N 1987 *J. Phys.* B **20** 3405–15
[7] Reid K L 2003 *Annu. Rev. Phys. Chem.* **54** 397–424
[8] Eland J H D 1979 *J. Chem. Phys.* **70** 2926–33
[9] Shigemasa E, Adachi J, Oura M and Yagishita A 1995 *Phys. Rev. Lett.* **74** 359–62
[10] Golovin A V, Heiser F, Quayle C J K, Morin P, Simon M, Gessner O, Guyon P M and Becker U 1997 *Phys. Rev. Lett.* **79** 4554–7
[11] Shigemasa E, Adachi J, Soejima K, Watanabe N, Yagishita A and Cherepkov N A 1998 *Phys. Rev. Lett.* **80** 1622–5
[12] Downie P and Powis I 1999 *Phys. Rev. Lett.* **82** 2864–7
[13] Downie P and Powis I 1999 *J. Chem. Phys.* **111** 4535–47
[14] Landers A *et al* 2001 *Phys. Rev. Lett.* **87** 013002
[15] Friedrich B and Herschbach D 1995 *Phys. Rev. Lett.* **74** 4623–6
[16] Stapelfeldt H and Seideman T 2003 *Rev. Mod. Phys.* **75** 543–57
[17] Larsen J J, Hald K, Bjerre N, Stapelfeldt H and Seideman T 2000 *Phys. Rev. Lett.* **85** 2470–3
[18] Filsinger F, Küpper J, Meijer G, Holmegaard L, Nielsen J H, Nevo I, Hansen J L and Stapelfeldt H 2009 *J. Chem. Phys.* **131** 064309
[19] Boll R *et al* 2014 *Faraday Discuss.* **171** 57–80
[20] Felker P M, Baskin J S and Zewail A H 1986 *J. Phys. Chem.* **90** 724–8
[21] Rosca-Pruna F and Vrakking M J J 2001 *Phys. Rev. Lett.* **87** 153902
[22] Renard V, Renard M, Guérin S, Pashayan Y T, Lavorel B, Faucher O and Jauslin H R 2003 *Phys. Rev. Lett.* **90** 153601
[23] Dooley P W, Litvinyuk I V, Lee K F, Rayner D M, Spanner M, Villeneuve D M and Corkum P B 2003 *Phys. Rev.* A **68** 023406
[24] Lee K F, Villeneuve D M, Corkum P B, Stolow A and Underwood J G 2006 *Phys. Rev. Lett.* **97** 173001
[25] Leibscher M, Averbukh I S and Rabitz H 2003 *Phys. Rev. Lett.* **90** 213001
[26] Horn C, Wollenhaupt M, Krug M, Baumert T, de Nalda R and Bañares L 2006 *Phys. Rev.* A **73** 031401
[27] Guérin S, Rouzée A and Hertz E 2008 *Phys. Rev.* A **77** 041404
[28] Bisgaard C Z, Poulsen M D, Péronne E, Viftrup S S and Stapelfeldt H 2004 *Phys. Rev. Lett.* **92** 173004
[29] Poulsen M D, Ejdrup T, Stapelfeldt H, Hamilton E and Seideman T 2006 *Phys. Rev.* A **73** 033405
[30] Ren X, Makhija V and Kumarappan V 2014 *Phys. Rev. Lett.* **112** 173602
[31] Ghafur O, Rouzée A, Gijsbertsen A, Siu W K, Stolte S and Vrakking M J J 2009 *Nat. Phys.* **5** 289–93
[32] Karamatskos E T *et al* 2019 *Nat. Commun.* **10** 3364
[33] Torres R *et al* 2007 *Phys. Rev. Lett.* **98** 203007
[34] Itatani J, Levesque J, Zeidler D, Niikura H, Pepin H, Kieffer J, Corkum P and Villeneuve D 2004 *Nature* **432** 867–71
[35] Pavičić D, Lee K F, Rayner D M, Corkum P B and Villeneuve D M 2007 *Phys. Rev. Lett.* **98** 243001
[36] Meckel M *et al* 2008 *Science* **320** 1478–82
[37] Pullen M G *et al* 2015 *Nat. Commun.* **6** 7262
[38] Küpper J *et al* 2014 *Phys. Rev. Lett.* **112** 083002
[39] Hensley C J, Yang J and Centurion M 2012 *Phys. Rev. Lett.* **109** 133202
[40] Yang J *et al* 2016 *Nat. Commun.* **7** 11232
[41] Kelkensberg F, Rouzée A, Siu W, Gademann G, Johnsson P, Lucchini M, Lucchese R R and Vrakking M J J 2011 *Phys. Rev.* A **84** 051404
[42] Rouzée A, Kelkensberg F, Siu W K, Gademann G, Lucchese R R and Vrakking M J J 2012 *J. Phys.* B **45** 074016

J. Phys. B: At. Mol. Opt. Phys. 56 (2023) 075101

F Brausse *et al*

[43] Thomann I, Lock R, Sharma V, Gagnon E, Pratt S T, Kapteyn H C, Murnane M M and Li W 2008 *J. Phys. Chem. A* **112** 9382–6

[44] Rouzée A, Harvey A G, Kelkensberg F, Brambila D, Siu W K, Gademann G, Smirnova O and Vrakking M J J 2014 *J. Phys. B* **47** 124017

[45] Marceau C, Makhija V, Platzer D, Naumov A Y, Corkum P B, Stolow A, Villeneuve D M and Hockett P 2017 *Phys. Rev. Lett.* **119** 083401

[46] Sutcliffe L H and Walsh A D 1961 *Trans. Faraday Soc.* **57** 873–83

[47] Cvitas T, Guesten H, Klasinc L, Novak I and Vancik H 1978 *Z. Nat.forsch. A* **32** 1528–32

[48] Yates B W, Tan K H, Bancroft G M and Tse J S 1986 *J. Chem. Phys.* **85** 3840

[49] Powis I, Dutuit O, Richard-Viard M and Guyon P M 1990 *J. Chem. Phys.* **92** 1643–52

[50] Gek Low K, Hampton P D and Powis I 1985 *Chem. Phys.* **100** 401–13

[51] Downie P and Powis I 2000 *Faraday Discuss.* **115** 103–17

[52] Bozek J, Bancro G, Cutler J, Tan K, Yates B and Tse J 1989 *Chem. Phys.* **132** 257–70

[53] McPherson A, Gibson G, Jara H, Johann U, Luk T S, McIntyre I A, Boyer K and Rhodes C K 1987 *J. Opt. Soc. Am. B* **4** 595–601

[54] Ferray M, L'Huillier A, Li X F, Lompre L A, Mainfray G and Manus C 1988 *J. Phys. B* **21** L31

[55] Eppink A T J B and Parker D H 1997 *Rev. Scient. Inst.* **68** 3477–84

[56] Toma E S and Muller H G 2002 *J. Phys. B* **35** 3435

[57] Aseyev S A, Ni Y, Frasinski L J, Muller H G and Vrakking M J J 2003 *Phys. Rev. Lett.* **91** 223902

[58] Dick B 2014 *Phys. Chem. Chem. Phys.* **16** 570–80

[59] Gianturco F A, Lucchese R R and Sanna N 1994 *J. Chem. Phys.* **100** 6464–71

[60] Natalense A P P and Lucchese R R 1999 *J. Chem. Phys.* **111** 5344–8

[61] Tatewaki H and Koga T 1996 *J. Chem. Phys.* **104** 8493–9

[62] Koga T, Yamamoto S, Shimazaki T and Tatewaki H 2002 *Theor. Chem. Acc.* **108** 41–45

[63] Cox A P, Duxbury G, Hardy J A and Kawashima Y 1980 *J. Chem. Soc. Faraday Trans.* 2 **76** 339–50

[64] Brausse F 2019 Shape resonances as a probe of an evolving nuclear and electronic structure in molecules *Dissertation* Freie University, Berlin

[65] Samson J A R and Stolte W C 2002 *J. Electron Spectrosc.* **123** 265–76

[66] Padial N T and Norcross D W 1984 *Phys. Rev. A* **29** 1742–8

[67] Marienfeld S, Fabrikant I I, Braun M, Ruf M W and Hotop H 2006 *J. Phys. B: At. Mol. Opt. Phys.* **39** 105

[68] Eland J H D, Feifel R and Hochlaf M 2008 *J. Chem. Phys.* **128** 234303

[69] Zare R N 1989 *Chem. Phys. Lett.* **156** 1–6

[70] Hamilton E, Seideman T, Ejdrup T, Poulsen M D, Bisgaard C Z, Viftrup S S and Stapelfeldt H 2005 *Phys. Rev. A* **72** 043402

[71] Bethe H A and Salpeter E E 1957 *Quantum Mechanics of One- and Two-Electron Atoms* (Berlin: Springer)

[72] Powis I 1997 *J. Chem. Phys.* **106** 5013–27

[73] Taylor J R 1972 *Scattering Theory: The Quantum Theory of Nonrelativistic Collisions* (New York: Wiley)

[74] Lucchese R R and Gianturco F A 1996 *Int. Rev. Phys. Chem.* **15** 429–66

[75] Stratmann R E and Lucchese R R 1992 *J. Chem. Phys.* **97** 6384–95

[76] Brausse F, Bach F, Krečinić F, Vrakking M J and Rouzée A 2020 *Phys. Rev. Lett.* **125** 123001